PHYSICAL REVIEW B **93**, 220301(R) (2016)

Generation mechanism of terahertz coherent acoustic phonons in Fe

T. Henighan,[1,2,*] M. Trigo,[1,3] S. Bonetti,[3] P. Granitzka,[3,4] D. Higley,[3,5,6] Z. Chen,[2,3] M. P. Jiang,[1,2] R. Kukreja,[3] A. Gray,[3] A. H. Reid,[3] E. Jal,[3] M. C. Hoffmann,[6] M. Kozina,[1,6] S. Song,[6] M. Chollet,[6] D. Zhu,[6] P. F. Xu,[7,8] J. Jeong,[7] K. Carva,[9,10] P. Maldonado,[10] P. M. Oppeneer,[10] M. G. Samant,[7] S. S. P. Parkin,[7,8] D. A. Reis,[1,3,5] and H. A. Dürr[3,†]

[1]*Stanford PULSE Institute, SLAC National Accelerator Laboratory, Menlo Park, California 94025, USA*

[2]*Physics Department, Stanford University, Stanford, California 94305, USA*

[3]*Stanford Institute for Materials and Energy Sciences, SLAC National Accelerator Laboratory, 2575 Sand Hill Road, Menlo Park, California 94025, USA*

[4]*Van der Waals-Zeeman Institute, University of Amsterdam, NL-1018 XE Amsterdam, The Netherlands*

[5]*Departments of Photon Science and Applied Physics, Stanford University, Stanford, California 94305, USA*

[6]*Linac Coherent Light Source, SLAC National Accelerator Laboratory, Menlo Park, California 94025, USA*

[7]*IBM Almaden Research Center, 650 Harry Road, San Jose, California 95120, USA*

[8]*Max-Planck Institute for Microstructure Physics, D-06120 Halle (Saale), Germany*

[9]*Faculty of Mathematics and Physics, Department of Condensed Matter Physics, Charles University in Prague, Ke Karlovu 5, CZ-12116 Prague 2, Czech Republic*

[10]*Department of Physics and Astronomy, Uppsala University, P. O. Box 516, S-75120 Uppsala, Sweden*

(Received 1 September 2015; revised manuscript received 11 May 2016; published 10 June 2016)

We use femtosecond time-resolved hard x-ray scattering to detect coherent acoustic phonons generated during ultrafast laser excitation of ferromagnetic bcc Fe films grown on MgO(001). We observe the coherent longitudinal-acoustic phonons as a function of wave vector through analysis of the temporal oscillations in the x-ray scattering signal. The width of the extracted strain wave front associated with this coherent motion is ∼100 fs. An effective electronic Grüneisen parameter is extracted within a two-temperature model. However, *ab initio* calculations show that the phonons are nonthermal on the time scale of the experiment, which calls into question the validity of extracting physical constants by fitting such a two-temperature model.

DOI: 10.1103/PhysRevB.93.220301

The speed limits for collective spin, electronic, and lattice motions are of fundamental interest and could have a profound effect on the ability to store and process information. So far the fastest manipulation of magnetic moments in ferromagnetic films has been achieved using femtosecond optical laser pulses [1–4]. Ultrafast demagnetization on time scales of only several hundred femtoseconds [1,5] is an important ingredient in all-optical magnetic switching [2,3]. Intriguingly, magnetic switching using strong magnetic and electric field pulses takes place on time scales similar to ultrafast demagnetization [6,7]. However, the underlying nonadiabatic motion of electrons and spins far from equilibrium and especially their coupling to the initially unperturbed lattice still poses a significant challenge to theory [5,8,9]. Typically, electron-phonon energy transfer following femtosecond laser heating in metals is described using the two-temperature model (2TM) [10]. This model has been used to explain ultrafast optical generation of lattice strain waves (coherent acoustic phonons) [10] which can manipulate [11] and coherently control [12] the magnetization orientation in ferromagnetic Ni films. Yet, the applicability of the 2TM on short time scales remains to be proven.

Femtosecond x-ray and electron scattering can provide a direct means for measuring the atomic-scale displacements associated with the propagating strain [13,14]. Nonetheless, experiments in metals have been limited primarily to observing the evolution of lattice temperature through the Debye-Waller factor [15] and the average lattice expansion through changes in the Bragg condition [14]. Although important for magnetoacoustic spin manipulation [11,12], laser-induced strain waves in magnetic 3*d* transition metals have been probed only optically, not with a direct structural probe such as diffraction.

Here, we use femtosecond hard x-ray pulses to probe the temporal evolution of quasielastic Bragg scattering from coherent acoustic phonons to directly detect the frequency content of ultrafast lattice strain waves generated during the femtosecond laser demagnetization of ferromagnetic Fe/MgO(001) films. The observed coherent oscillations can be unambiguously assigned to a coherent acoustic phonon wave packet with frequencies extending to 3.5 THz. Qualitative agreement is found when comparing the results to those of a 2TM which includes stress from the heated lattice and electronic subsystems. However, the validity of the 2TM, which assumes a thermal distribution for the phonons, is questionable considering the phonon thermalization time scales of ∼10 ps are longer than the time scales probed here. While previous works have noted that the electron distribution is likely nonthermal during the first ∼100 fs [16], the nonthermal behavior of the lattice has been largely ignored. Here, we show *ab initio* calculations which suggest that the highly nonthermal nature of the phonons influences the lattice stress and therefore the strain, and suggests that physical constants extracted by fitting to a 2TM model may only be effective parameters which do not represent the equilibrium values.

The Fe layer was deposited on a MgO substrate and capped with a 3 nm layer of MgO to prevent oxidation. Further details on sample fabrication are provided in the Supplemental Material [17]. Time-resolved magneto-optic Kerr experiments

*henighan@slac.stanford.edu
†hdurr@slac.stanford.edu

 ©2016 American Physical Society

established identical demagnetization behavior as observed previously [18]. The amount of demagnetization was less than 10% for the pump fluence of about 1 mJ/cm^2 used here. Optical pump x-ray probe measurements were performed at the XPP instrument [19] of the Linac Coherent Light Source free-electron laser with a pink beam at a 120 Hz repetition rate and $\sim 10^{12}$ photons per pulse. The photon energy was set to 7 keV, just below the iron K edge to avoid a fluorescence background. The x-ray scattering intensity was measured with an area detector [20]. Optical 800 nm pump pulses were 60 fs in duration. The time delay between the optical pump and x-ray probe was corrected for the x-ray arrival time jitter on a shot-by-shot basis [21]. A custom quadrupole electromagnet was used to control the film's in-plane magnetization direction [17]. However, we observed no dependence of the diffraction data on the in-plane magnetization direction. We operated in a reflection geometry with an x-ray (optical) cross section of 11×130 μm (300×390 μm) projected onto the sample at a grazing angle of 0.4° (2.4°) to match the x-ray penetration depth and film thickness. The finite optical x-ray crossing angle results in a negligible temporal smearing compared to the $\sim$100 fs resolution due to the finite durations of the pump and probe pulses. The optical pulses were p polarized with respect to the sample to minimize reflection losses. Sample motion was restricted to rotations about the sample normal to preserve the grazing x-ray incidence angle. The x-ray scattering was measured along the conventional $(01L)$ Bragg rod at different positions of $L = 1 + q_z$. In the kinematic limit, diffraction from ultrathin films with N atomic planes consists of discrete satellites spaced $\sim 1/N$ in reciprocal lattice units from the main peak [22]. We did not detect the individual satellite peaks for the 23 nm thick film used in this study because the x-ray spot size was kept large to avoid damage by the x-ray laser. However, a similarly prepared 12 nm film displayed clearly separated satellite features in reference measurements at the Stanford Synchrotron Radiation Lightsource (not shown), attesting to the excellent epitaxial quality of the Fe/MgO samples.

Figures 1(a)–1(d) show time-resolved diffraction traces (black lines and symbols) measured at different momenta transfers along the Bragg truncation rod $(011 + q_z)$. The truncation rod consists of discrete satellite peaks which are separated by $2\pi/d$ due to the finite film thickness d. The scattered intensity is integrated over a small region of reciprocal space encompassing 1–3 satellite peaks that are selected by the scattering geometry. Each trace shows high-frequency oscillations (up to 3.5 THz, as shown in the inset) accompanied by a more slowly oscillating envelope. This beating is a result of the integration over multiple satellites, each with a slightly different frequency. Figure 1(e) displays the dominant frequencies as a function of q_z. We find a linear relationship with the slope, closely matching the bulk longitudinal speed of sound of 5.13 nm/ps along ⟨001⟩ (red line) [23]. This clearly indicates that the temporal oscillations are related to laser-excited longitudinal-acoustic phonons traveling through the crystal along the film normal with wave vectors q_z. Figure 1 also shows that the phonons initially oscillate in phase, as expected for a coherent acoustic strain pulse generated by a stress that is nearly instantaneous when compared to a half period of the highest-frequency modes ($\lesssim$150 fs). The step

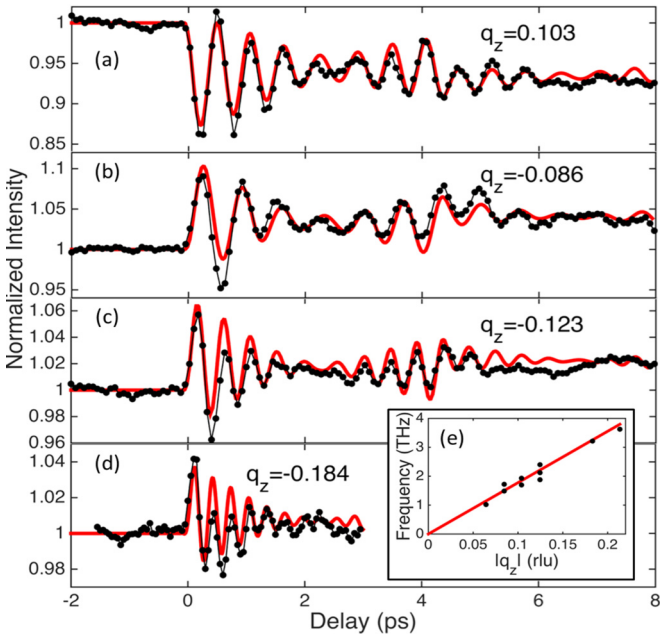

FIG. 1. Diffraction data (light lines and solid symbols) from a 23 nm thick Fe film as a function of optical pump–x-ray probe time delay for reduced wave vectors q_z (a)–(d). Heavy lines correspond to the best fit to the data for the laser-induced strain model described in the text. (e) shows the frequency of the x-ray intensity oscillations vs q_z (black dots) and the 5.13 nm/ps bulk speed of sound (red line).

just after 4 ps in Figs. 1(a)–1(c) corresponds to the acoustic propagation time across the thickness of the film. At this time a portion of the strain wave front originating at the free surface transmits into the substrate at the same time that the strain wave front originating at the substrate reaches the cap-layer Fe/MgO interface. As shown in the solid red curves of Figs. 1(a)–1(d), we find that the 2TM described below can closely reproduce the diffraction data.

Laser irradiation initially elevates electrons to higher energy levels. A combination of electron-electron and electron-phonon scattering will further shuffle the electron occupations and increase the phonon populations. Both the electron and phonon dispersions depend upon the strain, with energies typically being lowered upon stretching the crystal (tensile strain). As a result, laser-induced changes in electron and phonon populations will make introducing a strain energetically favorable. This new equilibrium is manifested as a stress, which is given by [24]

$$\sigma_{ij}(t,z) = \sum_{\mathbf{k}} \delta n_e(\mathbf{k},t,z) \frac{\partial E_{\mathbf{k}}}{\partial \eta_{ij}} + \sum_{\mathbf{k}} \delta n_p(\mathbf{k},t,z) \hbar \frac{\partial \omega_{\mathbf{k}}}{\partial \eta_{ij}}, \quad (1)$$

where η is the strain tensor, n_p and n_e are the phonon and electron populations (which are spatially and temporally dependent), and $\mathbf{k}$ is a composite index indicating both wave vector and branch/band. As has been shown previously, the spatial derivative of the stress acts as a driving force for acoustic vibrations [24]. Since the spot size far exceeds the penetration depth, we approximate the stress to be uniform in plane. Additionally, off-diagonal components of the stress tensor are disallowed when the film normal is parallel to a

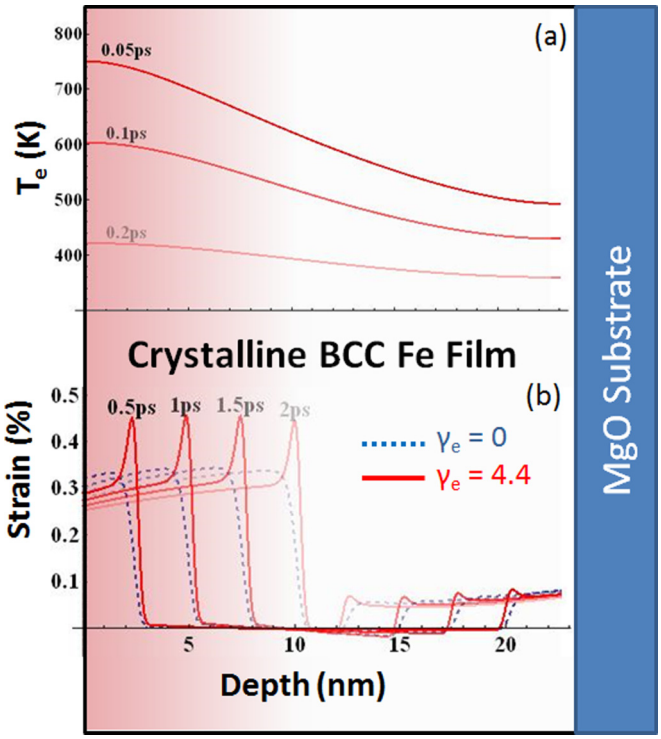

FIG. 2. Spatial profile of the electron temperature (a) and of the strain (b). In (b), the red solid lines (blue dashed lines) represent strain profiles obtained by fitting the experimental data to the model including (excluding) the effect of electronic stress, σ_e, from the laser-heated electronic system. The red shading schematically represents the electron temperature profile (which follows the laser penetration profile) just after excitation.

crystallographic high-symmetry direction [10,24]. Although transverse strain can be induced by spin-lattice coupling, we find it to be small in our case [17]. Thus we approximate σ_{zz} and thereby η_{zz} as nonzero, where z is along the film normal, giving rise to longitudinal acoustic atomic motion along z. This strain propagates in both directions and changes sign upon reflection from the free surface, giving rise to the sharp wave front in Fig. 2(b) [24].

A common approximation is to assume the phonon frequencies depend only on the change in volume and that the details of the volume change (e.g., uniaxial strain or isotropic expansion) are unimportant. In this case, anharmonicity is parametrized by the mode-dependent Grüneisen parameters defined for each mode as [25]

$$\gamma_{\mathbf{k}} = -\frac{V}{\omega_{\mathbf{k}}}\frac{\partial \omega_{\mathbf{k}}}{\partial V}, \tag{2}$$

where, again, $\mathbf{k}$ is a composite index indicating both wave vector and branch. Using this approximation and the expression above gives the following lattice stress,

$$\sigma_l(t,z) = \frac{1}{V}\sum_{\mathbf{k}} \gamma_{\mathbf{k}} \hbar \omega_{\mathbf{k}} \delta n_p(\mathbf{k},t,z). \tag{3}$$

We have dropped the tensor indices with the understanding that all strain and stress from hereon is the zz component.

It is common practice to assume that both the electron and lattice subsystems remain in local thermal equilibrium among themselves. The energy exchange between electrons and lattice is proportional to their temperature difference and the constant of proportionality is dubbed the electron-phonon coupling constant. In this so-called two-temperature model (2TM), we may rewrite the lattice and electronic stress as [26]

$$\sigma(t,z) = \sigma_e(t,z) + \sigma_l(t,z) = -\int_{T_e(t=0)}^{T_e(t,z)} \gamma_e C_e(T_e')dT_e' - \int_{T_l(t=0)}^{T_l(t,z)} \gamma_l C_l(T_l')dT_l', \tag{4}$$

where γ_l and γ_e are overall Grüneisen parameters, which are appropriately weighted sums of the mode-dependent Grüneisen parameters [25]. The overall Grüneisen parameters are often parameters extracted in fits to ultrafast strain measurements similar to those presented here [14,15,27].

The solid red lines of Fig. 1 are a fit to the data using the 2TM, where the stress is calculated according to Eq. (4). The Fe-MgO cap layer is treated as free, while strain transmission and reflection coefficients at the Fe-MgO substrate interface are calculated according to their acoustic impedance mismatch. Diffraction patterns from the transiently strained film were simulated using a kinematic-diffraction model which included the effects of heating (Debye-Waller factor) on the Bragg peak intensity and the finite attenuation length of the x rays (see the Supplemental Material [17]). Since all data were taken away from the Bragg condition, dynamical scattering effects could be neglected [28]. The only material parameter extracted from the model was γ_e. The other free parameters in the fit (absorbed fluence, x-ray grazing angle, film thickness, laser arrival time, and sample orientation) were allowed to vary within uncertainties of the measurement.

We find that including the electronic stress dramatically improves the agreement between data and simulation [27]. The best fits of calculated scattering from strain profiles and experimental data (red lines in Fig. 1) yield a γ_e of 4.4 (reduced χ^2 of 9.08) with the electron-phonon coupling constant G held fixed at 5.5×10^{18} W m^{-3} K^{-1} [29,30]. The errors in the scattering yield were estimated from the standard deviation of the measured scattering in Fig. 1 before the arrival of the laser pulse (negative time delays). Although $\gamma_e = 4.4$ is about twice the equilibrium value [31,32], we can achieve a similarly good fit $\gamma_e = 2.5$ if $G = 1 \times 10^{18}$ W m^{-3} K^{-1}. Parameters G and γ_e are strongly coupled in the fitting process, making it difficult to assign meaningful error bars to the fit results. The calculated strain profiles are shown in Fig. 2(b) for $\gamma_e = 0$ and 4.4 (corresponding to neglecting or including the electronic stress). The overshoot in the electronic temperature effectively drives higher-frequency, shorter-wavelength vibrational modes and modifies the frequency spectrum of the ensuing strain pulse via $\sigma_e(t,z)$ in Eq. (4), particularly at the highest frequencies. When we include the electronic stress, the resultant strain has sharper spatial features, corresponding to increased amplitudes of short-wavelength, high-frequency Fourier components.

While the fit of Fig. 1 seems convincing, the validity of the 2TM is questionable. The assumption of a thermal electron system for early times (~100 fs) is likely invalid [16] and previous works have speculated how this might affect the strain [33]. We have performed *ab initio* calculations which suggest that the phonon lifetimes exceed 10 ps [see Fig. 3(a)] and thus the phonons are expected to remain nonthermal for

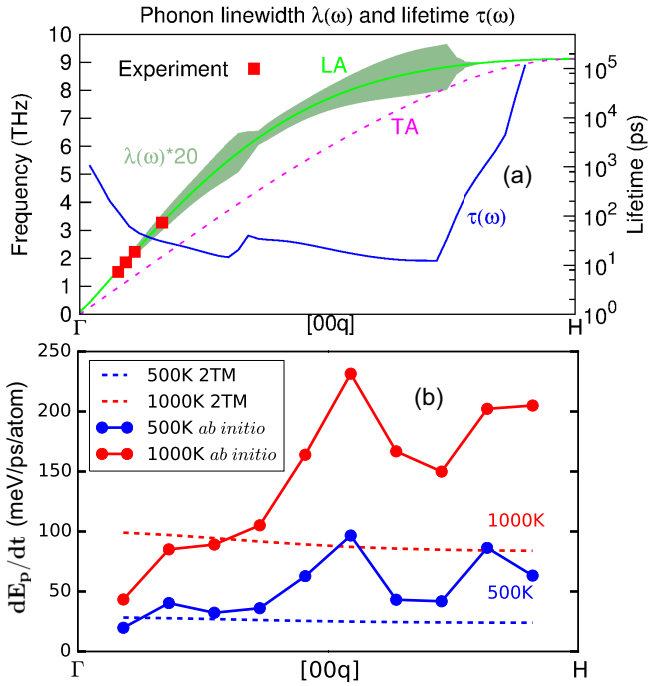

FIG. 3. (a) Calculated longitudinal (LA, green line) and transverse (TA, purple dashed line) acoustic phonon dispersions in bcc Fe along the Γ-H direction, including the LA inelastic phonon linewidth (green shaded area) and corresponding lifetime $\tau(\omega)$ (blue line). Red squares denote experimental values (from Fig. 1). (b) Rate of energy increase dE_p/dt for several phonon modes along Γ to H immediately after photoexcitation. The markers and lines are the *ab initio* calculations while the dashed curves are from the 2TM. Different colors denote different electron temperatures, i.e., different fluences. Note that $dE_p/dt = \hbar\omega dn_p/dt$ will dictate the rate of change of the stress from each mode, as given by Eqs. (1) and (3).

the entirety of our measurement. Further, using the recently derived Eliashberg theory for laser-heated electron systems [9], we compute *ab initio* the rate of energy transfer between the electrons and each phonon mode, $dE_p(T_e,\boldsymbol{k})/dt$, in Fe immediately after photoexcitation. Here, the electrons are treated as thermal with an elevated temperature, while the lattice is initially at 300 K. In Fig. 3(b), we show there is a clear deviation between the energy transfer rates predicted by the 2TM and *ab initio* calculations. This discrepancy implies that the 2TM's parametrization of the electron-phonon energy transfer into a single rate is an oversimplification. On the time scale of the electron cooling, the phonon modes do not exchange energy among themselves, and thereby must each individually come into equilibrium with the electrons. Thus there is not one but many electron-phonon energy transfer rates which will affect the temporal profiles of the electron cooling, lattice energy increase, and therefore the stress in accordance with Eq. (1). Specifically, in our case we find that the initial electron cooling is faster than predicted by the 2TM, which could give rise to an overshoot in the strain profile similar to that seen in Fig. 2 ($\gamma_e = 4.4$) even in the absence of electronic stress. While previous works have added a third temperature (three-temperature model) corresponding to the spin subsystem [1,5], we find this is unnecessary to fit the data. Additionally, a third temperature cannot remedy the exclusion of the nonthermal phonon dynamics, and physical constants extracted from such a fit are also only effective parameters within the model.

Better knowledge of the energy transfer between electrons and lattice would be relevant not only for strain generation, but also for ultrafast demagnetization and other situations where the 2TM is employed [5]. We note that time-resolved diffuse scattering can yield the evolution of nonequilibrium phonon populations [34,35].

In conclusion, we measure time-resolved x-ray diffraction from a Fe/MgO film following demagnetization by femtosecond optical irradiation. We observe THz frequency oscillations in diffracted intensity in regions of reciprocal space corresponding to scattering from the individual coherent longitudinal-acoustic phonon modes that make up the strain wave generated by the optical pulse. We find surprisingly close agreement when fitting this data with a two-temperature thermoelastic model in spite of the short time scales, which do not allow the lattice to thermalize. However, *ab initio* calculations of the phonon-mode-dependent Grüneisen parameters suggest that the nonthermal distribution of the energy in the phonon affects the stress exerted by the lattice, and therefore the strain. Thus, physical constants extracted by fitting the two-temperature model to data such as these may only yield effective parameters.

Research at SLAC was supported through the SIMES Institute which, as the LCLS and SSRL user facilities, is funded by the Office of Basic Energy Sciences of the US Department of Energy under Contract No. DE-AC02-76SF00515. K.C., P.M., and P.M.O. acknowledge support from the European Community's Seventh Framework Program (FP7/2007-2013) under Grant Agreement No. 281043, FemtoSpin, by the Swedish Research Council (VR) and SNIC. T.H. acknowledges support by the LCLS. S.B. and P.M.O. acknowledge support from the Knut and Alice Wallenberg Foundation. K.C. acknowledges support from the Czech Science Foundation (Grant No. GJ15-08740Y).

[1] E. Beaurepaire, J.-C. Merle, A. Daunois, and J.-Y. Bigot, Phys. Rev. Lett. **76**, 4250 (1996).

[2] C. D. Stanciu, F. Hansteen, A. V. Kimel, A. Kirilyuk, A. Tsukamoto, A. Itoh, and T. Rasing, Phys. Rev. Lett. **99**, 047601 (2007).

[3] I. Radu, K. Vahaplar, C. Stamm, T. Kachel, N. Pontius, H. A. Dürr, T. A. Ostler, J. Barker, R. F. L. Evans, R. W. Chantrell *et al.*, Nature (London) **472**, 205 (2011).

[4] C.-H. Lambert, S. Mangin, B. C. S. Varaprasad, Y. Takahashi, M. Hehn, M. Cinchetti, G. Malinowski, K. Hono, Y. Fainman, M. Aeschlimann *et al.*, Science **345**, 1337 (2014).

[5] B. Koopmans, G. Malinowski, F. Dalla Longa, D. Steiauf, M. Fähnle, T. Roth, M. Cinchetti, and M. Aeschlimann, Nat. Mater. **9**, 259 (2010).

[6] C. H. Back, R. Allenspach, W. Weber, S. S. P. Parkin, D. Weller, E. L. Garwin, and H. C. Siegmann, Science **285**, 864 (1999).

[7] S. J. Gamble, M. H. Burkhardt, A. Kashuba, R. Allenspach, S. S. P. Parkin, H. C. Siegmann, and J. Stöhr, Phys. Rev. Lett. **102**, 217201 (2009).
[8] A. J. Schellekens and B. Koopmans, Phys. Rev. Lett. **110**, 217204 (2013).
[9] K. Carva, M. Battiato, D. Legut, and P. M. Oppeneer, Phys. Rev. B **87**, 184425 (2013).
[10] O. B. Wright, Phys. Rev. B **49**, 9985 (1994).
[11] J.-W. Kim, M. Vomir, and J.-Y. Bigot, Phys. Rev. Lett. **109**, 166601 (2012).
[12] J.-W. Kim, M. Vomir, and J.-Y. Bigot, Sci. Rep. **5**, 8511 (2015).
[13] D. A. Reis and A. M. Lindenberg, in *Light Scattering in Solids IX* (Springer, Berlin, 2007), pp. 371–422.
[14] S. Nie, X. Wang, H. Park, R. Clinite, and J. Cao, Phys. Rev. Lett. **96**, 025901 (2006).
[15] X. Wang, S. Nie, J. Li, R. Clinite, M. Wartenbe, M. Martin, W. Liang, and J. Cao, Appl. Phys. Lett. **92**, 121918 (2008).
[16] E. Carpene, Phys. Rev. B **74**, 024301 (2006).
[17] See Supplemental Material at http://link.aps.org/supplemental/10.1103/PhysRevB.93.220301 for more information on sample preparation, strain modeling, and fitting procedures.
[18] E. Carpene, E. Mancini, C. Dallera, M. Brenna, E. Puppin, and S. De Silvestri, Phys. Rev. B **78**, 174422 (2008).
[19] M. Chollet, R. Alonso-Mori, M. Cammarata, D. Damiani, J. Defever, J. T. Delor, Y. Feng, J. M. Glownia, J. B. Langton, S. Nelson *et al.*, J. Synchrotron Radiat. **22**, 503 (2015).
[20] P. Hart, S. Boutet, G. Carini, M. Dubrovin, B. Duda, D. Fritz, G. Haller, R. Herbst, S. Herrmann, C. Kenney *et al.*, Proc. SPIE **8504**, 85040C (2012).
[21] M. Harmand, R. Coffee, M. R. Bionta, M. Chollet, D. French, D. Zhu, D. M. Fritz, H. T. Lemke, N. Medvedev, B. Ziaja *et al.*, Nat. Photonics **7**, 215 (2013).
[22] B. E. Warren, *X-Ray Diffraction* (Courier Corporation, North Chelmsford, MA, 1969).
[23] W. M. Haynes, *CRC Handbook of Chemistry and Physics* (CRC Press, Boca Raton, FL, 2013).
[24] C. Thomsen, H. T. Grahn, H. J. Maris, and J. Tauc, Phys. Rev. B **34**, 4129 (1986).
[25] N. Ashcroft and N. Mermin, *Solid State Physics* (Cengage Learning, Boston, 2011).
[26] C. Thomsen, J. Strait, Z. Vardeny, H. J. Maris, J. Tauc, and J. J. Hauser, Phys. Rev. Lett. **53**, 989 (1984).
[27] M. Nicoul, U. Shymanovich, A. Tarasevitch, D. von der Linde, and K. Sokolowski-Tinten, Appl. Phys. Lett. **98**, 191902 (2011).
[28] B. W. Batterman and H. Cole, Rev. Mod. Phys. **36**, 681 (1964).
[29] Z. Lin, L. V. Zhigilei, and V. Celli, Phys. Rev. B **77**, 075133 (2008).
[30] Z. Lin and L. V. Zhigilei, Electron-phonon coupling and electron heat capacity in metals at high electron temperatures, http://www.faculty.virginia.edu/CompMat/electron-phonon-coupling/, accessed 2014-09-30.
[31] T. H. K. Barron, J. G. Collins, and G. K. White, Adv. Phys. **29**, 609 (1980).
[32] G. K. White, Proc. Phys. Soc. **86**, 159 (1965).
[33] E. Tzianaki, M. Bakarezos, G. D. Tsibidis, Y. Orphanos, P. A. Loukakos, C. Kosmidis, P. Patsalas, M. Tatarakis, and N. A. Papadogiannis, Opt. Express **23**, 17191 (2015).
[34] M. Trigo, J. Chen, V. H. Vishwanath, Y. M. Sheu, T. Graber, R. Henning, and D. A. Reis, Phys. Rev. B **82**, 235205 (2010).
[35] T. Chase, M. Trigo, A. Reid, R. Li, T. Vecchione, X. Shen, S. Weathersby, R. Coffee, N. Hartmann, D. Reis *et al.*, Appl. Phys. Lett. **108**, 041909 (2016).